Ground Studies of Ionospheric Plasma Interactions with a High Voltage Solar Array

H. Kuninaka,* Y. Nozaki,† S. Satori,† and K. Kuriki‡
Institute of Space and Astronautical Science, Yoshinodai, Sagamihara, Kanagawa, Japan

High voltages are required for the efficient transfer and generation of high levels of electrical power. The higher the voltage becomes, the more seriously space plasma interactions impact a spacecraft. The interactions are particularly severe for solar arrays when interconnects between the solar cells are exposed to the space plasma. Even though the NASA space station will employ only 160 V, such a high voltage has never been applied to an operational solar array in space. In this paper, a similarity law for ion collection of solar arrays was derived from the governing equations, and a scaled experiment based on the similarity law was conducted on the ground. New interactions associated with the ion force and surface degradation by sputtering were confirmed, as had been predicted in a preceding paper. These phenomena must be taken into account in determining the dynamics of a spacecraft and the endurance of solar arrays when a high voltage solar array will be operated in orbit.

Nomenclature

B = strength of magnetic field
c = unit vector of cord
D = length of sheath
d = displacement of pendulum
d = unit vector of drag $= -u$
E = kinetic energy
e = charge of electron
F = force
F = ion force vector
g = gravitational acceleration
h = length from hinge in pendulum
I = moment of inertia
k = Bolzmann constant
L = length of High Voltage Solar Array (HVSA)
l = mean free path
l = unit vector of lift $= d \times p$
m = mass
N = particle density
n = unit normal of HVSA surface
P = scaling parameter, defined in Eq. (7)
p = unit vector of side slip force; $= u \times n/(|u \times n|)$ ($\alpha \neq \pm 90$ deg); $= s(\alpha = \pm 90$ deg)
R = Larmor radius
s = unit vector of span
T = temperature
U = orbital velocity
u = unit vector of orbital velocity
V = potential
v = particle velocity
x = variable in space
α, β = angles of attack and side slip
γ = emissive yield
η = normalized electron temperature $= kT_e/E_i$
θ = normalized electron temperature, defined in Eq. (8)
λ_D = Debye length
ξ = normalized length $= L\Omega/U_i$
τ = period of pendulum
ϕ = normalized potential $= -eV/E_i$
ψ = angle measured from normal
Ω = ion plasma frequency

Subscripts

A = solar array
bs = backscattering
e = electron
f = application point in pendulum
i = ion
j = jth part in pendulum
n = neutral particle
s = sensing point in pendulum
sp = sputtering
w = weight in pendulum
$'$ = as for drift velocity

Received Nov. 21, 1988; revision received Aug. 3, 1989.

*Research Associate. Member AIAA.
†Graduate Student.
‡Professor. Associate Fellow AIAA.

Introduction

IN parallel with the increase of human activities in space, a larger amount of electrical power is required. The space power issues that may impose constraints on space activities are acquisition, storage, transfer, conversion, and waste. Associated with high electrical power, efficient generation and transfer are enhanced by high voltage, as with ground systems. High voltage reduces the mass of power cables and eliminates the loss in dc-dc converters. In illustration of such space systems, the Skylab in 1973 adopted about 75 V as a bus voltage, whereas the NASA space station will employ 160 V. The higher the voltage becomes, however, the more seriously the space plasma interactions impact the spacecraft.[1] In low Earth orbit (LEO), the impact will be particularly severe for solar arrays when the interconnections between the solar cells are exposed to the ionospheric plasma. If the ionospheric plasma interferes significantly with the solar array, some protection may be required; e.g., insulation of the interconnections. Excessive protection, however, will result in endurance, weight, and cost penalties and will endanger the usefulness of the solar array. The High Voltage Solar Array (HVSA) Experiment[2] onboard the Japanese reusable spacecraft, Space Flyer Unit, is currently being developed in order to investigate such plasma interactions. The first flight test is planned for early 1993, when solar activity will be near maximum, so that a particularly severe environment will exist. For these reasons, the ionospheric plasma interactions with an HVSA is a timely topic and worthy of being studied as one of the key technologies for space activities in the near future.

The interactions of an HVSA with space plasma can be viewed as follows. Ions and electrons are collected by the HVSA through a space charge sheath, which is formed around the conductive surface of the HVSA at some potential relative to the plasma potential. This plasma current results in leakage

of the power from the HVSA. The occasional release of electric charge accumulated on a floating part causes electromagnetic interference with onboard electronics. These interactions are predicted by many investigators[3] and have been verified by ground experiments[4] and short-duration rocket experiments.[5] In the previous works,[3,4] the HVSAs were assumed to be stationary so that ions have no drift speed. Numerical simulations by the authors[6] for a negatively biased HVSA moving at orbital velocity have revealed new interactions: spacecraft drag and solar cell erosion due to momentum and mass exchanges between the HVSA and the plasma. The potential distribution appearing on interconnections of solar cells is dependent on the electrical circuit of the HVSA. On the other hand, the potential relative to the ionospheric plasma adjusts itself so as to collect no net plasma current because the HVSA's circuit is grounded on the spacecraft body and is floating. The electron impinges on a positive sheath of the HVSA with its thermal velocity, whereas the ion does on a negative sheath with the satellite orbital velocity. The difference in the current densities between the two species makes the potential on almost all the parts of the HVSA's circuit lower than the plasma potential. Ions are collected strongly depending on the HVSA's attitude relative to the ionosphere in contrast with nondirectional collection. Such ion collection is essential to the interactions of the HVSA with the ionospheric plasma because the ion properties determine the leakage current, the ion drag, and the surface degradation.

A ground experiment simulation using a real-scale HVSA is currently not realistic if the dimensions of available space chambers and requirements for uniform plasma flow, ultrahigh vacuum, and so forth are considered. It is, however, possible to use a miniature model based on similarity laws in the laboratory.[7] The scale experiment has the following advantages in contrast to the real-size experiment on the ground.

1) A huge space chamber and ultrahigh vacuum are unnecessary.

2) It is possible to produce uniform plasma flow for a miniature model.

3) Interaction phenomena can be visualized due to a dense plasma.

4) Capability to make an artificial test environment is useful for verifying the similarity laws.

We can reduce influence of the space chamber wall in the ground experiment since the dense plasma electrically shields a solar array model from the wall. The objectives in the present work are to establish the similarity law and a technique for scaling the experiment and to investigate the interactions of the HVSA with the ionospheric plasma using this technique.

Similarity Law

The plasma parameters in LEO at 500-km altitude where the space station is designed to orbit are summarized in Table 1.[8] Under these conditions the electron thermal velocity v_e, the satellite orbital velocity U, and the ion thermal velocity v_i satisfy the following relation:

$$v_e \gg U \gg v_i \tag{1}$$

so that ions are approximated as impinging on the satellite with a velocity U whereas electrons impinge with a velocity v_e. The characteristic length L_A, assumed to be the 5-m HVSA span, is shorter than the mean free path l, whereas it is longer than the plasma Debye length λ_D. These conditions permit the particles to be regarded as a collisionless plasma near the HVSA.

$$l \gg L_A \gg \lambda_D \tag{2}$$

The ion kinetic energy E_i is smaller than the absolute maximum array voltage $|V_A|$ and larger than the electron thermal energy kT_e:

$$e|V_A| \gg E_i \gg kT_e \tag{3}$$

where the voltage V_A applied to the HVSA is assumed to be -500 V. The ion Larmor radii R_i' and R_i for the drift and thermal velocities are larger than L_A whereas that of electron R_e, with reference to the thermal velocity, is smaller. Therefore, the geomagnetic field has little effect on the ion collection by the HVSA in LEO.

$$R_i' \gg R_i > L_A \gg R_e \tag{4}$$

As stated previously, the ion properties rather than those of the electrons have a more significant effect on the interactions of the HVSA. In this work, the interactions of the HVSA with the ionospheric plasma are studied with respect to ion collection by assuming almost all the area of the HVSA to have negative potential relative to the plasma. The assumptions are summarized as follows:

1) The ionospheric environment is regarded as collisionless plasma with no magnetic field.

2) The electrons are in thermal equilibrium and ions have zero temperature.

3) The HVSA acts as a simple plate that has a conductive surface on one side and has an insulated surface on the other.

We should comment on the last assumption. In general, the solar cell is mostly covered with glass, which tends to close to the plasma potential. The solar array potential appears only at the interconnections and is covered with a space charge sheath. Since the sheath thickness is larger than the space between the interconnections, the solar array is entirely covered with a single sheath. Observed from the outside of the sheath, the HVSA behaves electrically as a single conductive plate. Needless to say, the potential structure near the surface of the HVSA is complicated owing to the existence of both the insulators and conductors.[9] To accomplish our first objective, to establish the similarity law and the scale experiment, it is advantageous to use a conductive plate with an insulated back

Table 1 Comparisons of plasma environment and scaling parameters between conditions in LEO and in laboratory

	T_e	N_e	N_n	E_i	B	m_i
LEO	0.2 eV	5×10^5 cm^{-3}	—	5 eV	0.3 G	16.6
Laboratory	2.2 eV	5×10^9 cm^{-3}	7×10^{12} cm^{-3}	36 eV	9 G	40

	Eq. (1) $v_e \gg U_i$	Eqs. (2), (12) $l_{ie}, l_{in}, R_i' \gg L_A \gg \lambda_D$	Eq. (3) $\|V_A\| \gg E_i \gg kT_e$
LEO	250 km/s $\gg$ 7.6 km/s	4 km, —, 40 m $\gg$ 1.6 m $\gg$ 0.5 cm	500 V $\gg$ 5 eV $\gg$ 0.2 eV
Laboratory	880 km/s $\gg$ 13 km/s	30 m, 40 cm, 6 m $\gg$ 4.4 cm $\gg$ 0.2 mm	3.6 kV $\gg$ 36 eV $\gg$ 2.2 eV

	L_A	V_A	P	θ
LEO	1.6 m	-500 V	4.9	4×10^{-4}
Laboratory	4.4 cm	-3.6 kV	4.9	6×10^{-4}

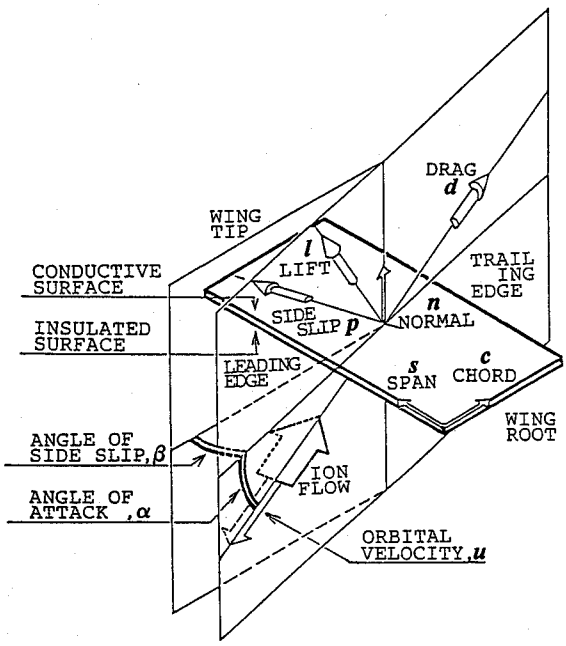

Fig. 1 Coordinates system of solar array and ion flow.

for simplification. Some cautions, however, must be added in directly applying the results to a real HVSA. Recently, another type of the solar cell that has a cover glass coated with a conductive paint has been developed.[10] In such a case, the solar array is strictly a conductor because the conductive cover glass is connected electrically to one side of the cell electrodes.

The angles of attack α and side slip β based on the ion flow are shown in Fig. 1. The drag d, side slip p, and lift l are also seen there. They are defined mathematically by unit vectors of orbital velocity u, normal on the conductive surface n, and span from the wing root to tip s as follows:

$$\sin\alpha = -(u,n), \qquad \text{Drag} = (F,d)$$

$$\sin\beta = -(p,c), \qquad \text{Lift} = (F,l)$$

$$\text{Side Slip} = (F,p) \tag{5}$$

The unit side slip vector p is dependent on the angle of attack α. For $\beta = 0$, the conditions at $\alpha = -90$, 0, and $+90$ are called "ram," "airplane," and "wake" modes, respectively, with regard to the relation between the conductive surface and the plasma flow. The position on the HVSA is indicated by the spanwise and chordwise locations in percentage of the respective array dimensions.

The Poisson and ion kinetic equations imply the following in one dimension, neglecting of the electron term:

$$\frac{d^2V}{dx^2} = -\frac{e}{\epsilon} N_e U_i \sqrt{\frac{m_i}{-2eV}} \tag{6}$$

Equation (6) becomes the Child-Langmuir equation in general. By respective normalizations of V and x by V_A and L_A, one derives one of the scaling parameters, that is, P:

$$P \equiv \frac{L_A^2 e N_e U_i}{\epsilon |V_A|^{1.5}} \sqrt{\frac{m_i}{2e}} \tag{7}$$

$$\theta \equiv \frac{kT_e}{e|V_A|} \tag{8}$$

The θ represents the effect of the electron term that is neglected in Eq. (6). The P and θ are scaling parameters because HVSAs having the same P and θ are governed by the same formula. The P parameter is significant to the interaction of the HVSA because inequality (3) assures that the θ is small enough to neglect the electron term in the Poisson equation. The P can then be converted into

$$P = 4/9(L_A/D_i)^2 \tag{9}$$

and also can be considered to the normalized perveance, which is used in the theory of vacuum tubes. In addition, Eqs. (7) and (8) can be rewritten using ϕ, ξ, and η, which are used in Ref. (6), as

$$P = (2\xi_A^2)/(\phi_A^{1.5}) \tag{10}$$

$$\theta = \eta/(\phi_A) \tag{11}$$

The experiment simulation, using a small scale model,[7] was conducted in the laboratory using a more dense plasma than that in LEO as required by the similarity law. In the simulated plasma environment, inequalities (1), (2), and (3) must be satisfied. Among the several mean free paths, that for ion-neutral collisions is the most critical in satisfying the inequality (2) in the laboratory. As for the magnetic field, assumption (2) requires the following relation instead of inequality (4):

$$R_i' \gg L_A \tag{12}$$

The P parameter in the laboratory must be equal to that in LEO. The normalized electron temperature, θ, does not have to be equal as long as inequality (3) is met. In other words, the plasma flow is supersonic because the characteristics of the electrons have little effect on ion collection by the HVSA.

Numerical Simulation

The fundamental equations were solved iteratively until a self-consistent solution was obtained using a particle tracking method. An HVSA was modeled to be a simple conductive plate biased uniformly with an insulated back in comparison to the scale experiment. The current through the HVSA was estimated with a 10% addition to the ion current in the consideration of secondary electron emission from the conductor.[11] The ion drag and lift were calculated using accommodation coefficients. More details are given in Ref. (6).

Scaled Experiment

Vacuum System and Plasma Source

All simulations were carried out in a space chamber, which is 2.8 m in length and 1.5 m in diameter. The space chamber, made of stainless steel and electrically grounded, was evacuated by an oil diffusion pump of pumping speed 4,300 l/s. The diffusion pump was backed by an oil rotary pump of 3,000 l/min pumping speed. The pressure in the space chamber was around 2×10^{-6} torr before the working gas was supplied.

The plasma flow was generated by a steady-state Hall type accelerator,[12] which ionizes gas and accelerates plasma by the Lorentz force due to the Hall current and an external magnetic field. The operational conditions were typically 2 A in discharge current, 105 V in discharge voltage, 0.85 mg/s in mass flow rate of the working gas, argon, and 2×10^{-4} torr in back pressure. The plasma parameters were measured by a Langmuir probe, a retarding potential analyzer, a time of flight method, an optical multichannel analyzer (OMA), and a Hall sensor. The spectrum of the plasma plume was observed by OMA, and only lines of AI and AII were identified. The properties of the plasma produced at 13 cm downstream from the exit of the accelerator are listed in Table 1, which also shows comparisons between the conditions in LEO and the laboratory. According to the similarity law, the plasma generated in the space chamber achieves the conditions stated in the preceding section. A solar array of 1.6 m in length and a bus voltage of 500 V in LEO can be simulated by a model of 4.4-cm length and 3.6 kV potential in the laboratory because

of the P parameter. It was estimated from the ionization probability that the influence exerted on the plasma by the solar array model does not provide additional ionization of the streaming gas.

Solar Array Models

The characteristics of total ion current, ion drag and lift, and potential distribution were measured using a simple tungsten plate with one side insulated by a boron-nitride plate of 4.4 cm length squared, which is called the "baseline" model. So as to ensure the validity of the similarity law, a "small" model of 2 cm in length squared was also used.

The model, divided into 3×3 electrodes, was used to measure the ion current distribution. It consisted of nine tungsten plates and a boron-nitride substratum of 4.4 cm square and was named the "segmented" model.

All versions of the solar array model except that used for the drag and the lift measurements could be located and rotated with respect to the flow by an X-Y table combined with a stepping motor in the space chamber.

Electrical Circuit

The models were biased uniformly as low as -3 kV with reference to the ground with a constant voltage power supply with 10 V accuracy. The total ion current collected by the models was monitored by a shunt resistor within 1% accuracy. In the measurement of the ion current distribution using the segmented model biased uniformly, the ion current signal from each segment was transferred via a photocoupler, the SHARP PC511, to a pen recorder. Every photocoupler was calibrated separately for its characteristic input current and output voltage taking nonlinearity into account. The accuracy of the current measurement is ±3% due to the ambient temperature fluctuation. The potential drop across the photocoupler with a protection circuit is less than 3 V.

Drag and Lift Measurement

The characteristics of the ion drag and lift were measured by the pendulum method. The baseline model was suspended by ceramic rods and tungsten wire from the ceiling of the space chamber and provided with power through a flexible cable insulated with Teflon. The swing of the pendulum system along the direction of the drag or the lift was detected by an optical displacement sensor, the KEYENCE PA-1810, with an accuracy of 1 μm. This pendulum method was calibrated by two ways. One way was to find a functional relation between the displacement of the pendulum system and known force using a load cell, the KYOWA 120T-5B. The second way was to find the moment of inertia about the pendulum system from the change of swing period by the addition of a known weight. The dynamics of a pendulum are represented by the following equations:

$$Fh_f = \frac{gd}{h_s}\left(\Sigma m_j h_j + m_w h_w\right) \tag{13}$$

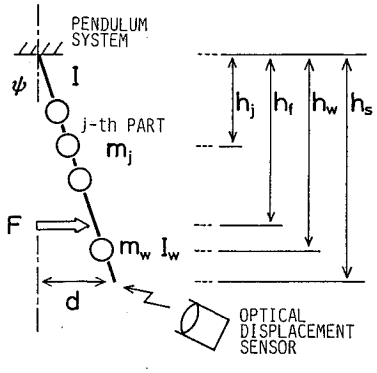

Fig. 2 Notations of the pendulum system for force measurement.

$$\tau = 2\pi\sqrt{\frac{I + I_w + m_w h_w^2}{g(\Sigma m_j h_j + m_w h_w)}} \tag{14}$$

where the notations are seen in Fig. 2. The τ is functionally dependent on h_w for a specific weight. Equation (14) is converted into

$$h_w\left[g\left(\frac{\tau}{2\pi}\right)^2 - h_w\right] = -\frac{\Sigma m_j h_j}{m_w}g\left(\frac{\tau}{2\pi}\right)^2 + \frac{I + I_w}{m_w} \tag{15}$$

The characteristic of h_w $[g(\tau/2\pi)^2 - h_w]$ and $g(\tau/2\pi)^2$ reveals the $\Sigma m_j h_j$ by measuring the swing period with variable h_w using the known weight so that the force F can be calculated by Eq. (13) with the measured value d. The two calibrated results coincide well with each other. The friction of the pendulum system estimated from its damping characteristics is 0.5 μN. The measured data have an uncertainty of less than ±5% and ±20 μN.

Observation by Video Camera

The experiment simulation using the similarity law enabled the observation of interaction phenomena by a conventional video camera owing to the brightness of the dense plasma. This is one of the advantages of the scale experiment. Their visualization in a real-size experiment using diluted plasma requires a special instrument, for example, a low-light TV camera. Using a digital image converter, the video image was processed into contours of equal brightness.

Emissive Probe

The potential distribution around the baseline model was measured by an emissive probe mounted on an X-Y table, which was driven by a microcomputer with 0.1-mm resolution. The probe was made of thoriated tungsten wire of 0.2 mm in diameter and heated by a 5-A current. The probe current was measured with respect to probe location at constant potential, in contrast to the usual method of emissive probe use. When the probe passes through the position having the same potential as that of the probe, the emission current from the probe changes drastically to near zero. Such a position was defined to correspond to the maximum inclination of the current profile with the background plasma current subtracted. The results have errors of ±1.3 mm in location and ±5 V in potential due to the finiteness of the probe size, the accuracy of the X-Y table, and the potential variation in the probe. The emissive current was about 3 mA, which was much less than the total current collected by the solar array model.

Numerical and Experimental Results

Characteristics of Ion Current

The ion current dependences on the P parameter for the calculation and the experiment are shown in Fig. 3 in the ram and the airplane modes. This figure contains the data for an L_A of 2 and 4.4 cm, V_A from -0.5 to -3 kV, N_e from 2.4×10^9 to 1.7×10^{10} cm^{-3}, and E_i from 30 to 40 eV. The ion current is normalized to the ion current ratio by the unbiased ram current. The circle and cross symbols represent the results for the baseline and the small models with the tungsten electrode, respectively. The data for the two models overlap smoothly with each other and agree well with the solid curve representing the numerical result. By increasing the P parameter, the ion current ratio for the ram mode seems to converge to unity and that for the airplane mode to zero. The data in both the ram and the airplane modes seem to converge as the P parameter decreases. The ion current characteristic is approximately proportional to -0.5 power of the P parameter for the airplane case.

The dependence of the ion current on the angle of attack is shown in Fig. 4 at -2 kV, the array potential. The ion currents are normalized by the unbiased ram current for each model. The experimental results for the baseline and the small

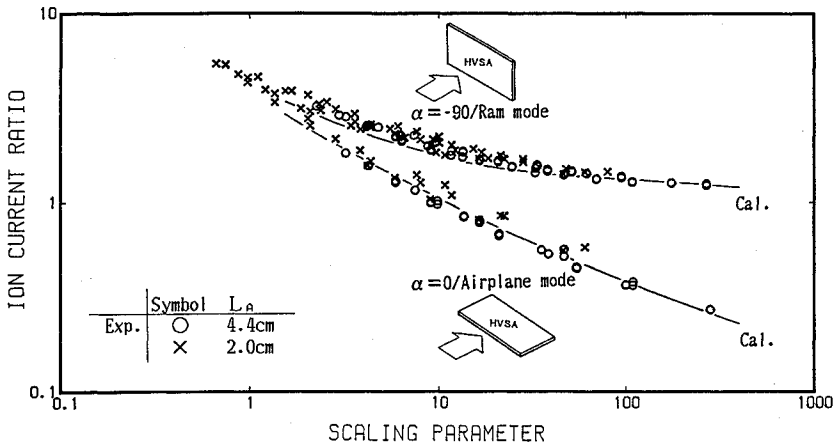

Fig. 3 Dependence of the ion current ratio on the *P* parameter in the ram and airplane modes; circles, cross symbols, and solid curves represent results obtained by the baseline, the small models, and the calculation, respectively.

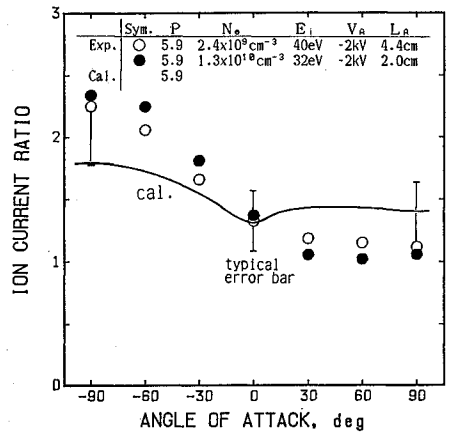

Fig. 4 Dependences of ion current ratio on angle of attack at −2 kV array voltage; circles, cross symbols, and solid curves represent results obtained by the baseline, the small models, and the calculation, respectively.

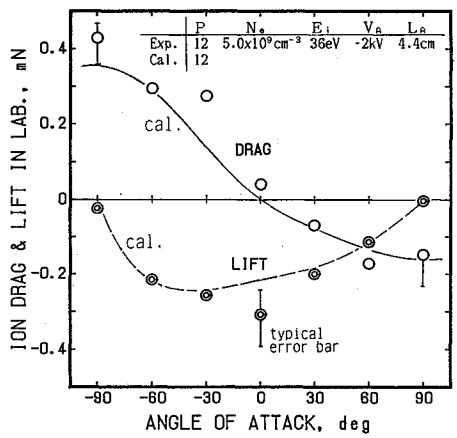

Fig. 5 Dependences of ion drag and lift on angle of attack at −2 kv array voltage; open and solid symbols represent drag and lift for the experiment, respectively; solid and broken curves are obtained by the calculation.

models, which correspond to a *P* parameter of 5.9, agree well with each other, and the numerical result is within the accuracy represented by the error bars.

Characteristics of Ion Drag and Lift

The experimental results for the ion drag and lift are compared as a function of the angle of attack in Fig. 5 and −2 kV array potential with the numerical one. They were obtained by measuring the displacement of the pendulum system in the biased condition from the floating condition, which had already been affected by the aerodynamic force. The ion lift has a negative sign due to the definition in Eqs. (5) and is never produced in the ram and the wake modes owing to the symmetry of the model. The ion drag shows a maximum for the ram mode and turns negative, namely, acts as thrust at positive angles of attack.

Measurement of Ion Sheath

A dark area around the model was observed in the bright ion beam and changed its configuration depending on the array potential, the plasma density, and the angle of attack. The baseline model with a copper electrode was observed from the direction perpendicular to both the ion beam vector and the normal vector of the array surface as shown in Fig. 6. The experiment, using a copper electrode, enabled the observation of the dark area because of the dimness on the electrode surface. The dark area is thin on the ram side and thick in the wake though the array is biased uniformly. The dark area enlarges with an increase of the array potential and with a decrease of the plasma density because of lack of plasma shielding.

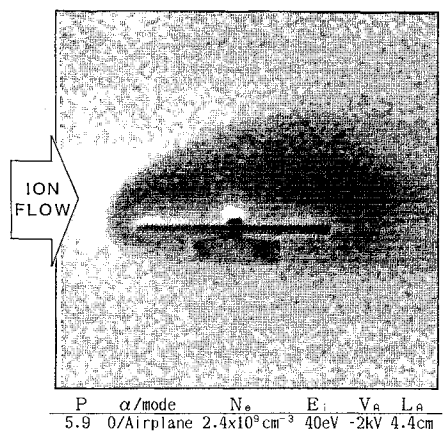

Fig. 6 Dark area around the solar array model in the airplane mode observed by a video camera.

Figures 7–9 represent the experimental results for the emissive probe and are superimposed on the numerical results for equipotential contours in the ram, the airplane, and the wake modes. The positions corresponding to −40 and −400 V with respect to the plasma potential were identified from the emissive probe data in the cross section at 50% span. Each cross bar represents the spatial error.

Ion Current Distribution

The model with tungsten or molybdenum glowed on its surface in the ion beam when it was biased. Its luminous pattern changed depending on the plasma density, the array potential, and the angle of attack. It is considered to correspond to the current density distribution. The luminous pattern in the wake mode is shown in Fig. 10. The arched areas without luminescence existed on all the edges of the model and became larger with increasing array potential and decreasing plasma density. A circular shadow on the center of the model in Fig. 10 is the head of a screw used to attach the electrode. The numerical simulation predicted a similar figure to Fig. 10 as shown in Fig. 11.

After many operations in the wake mode, a flaw pattern similar to that of the luminosity and a hole near each corner were observed on the tungsten electrode surface. Frequent ion collisions apparently eroded the tungsten electrode and formed holes on it by sputtering.

The ion current distribution was measured with the segmented model at each angle of attack. The experimental result in the wake mode is compared in Fig. 12 with the calculated one for a P parameter of 5.9. The ion current is normalized by that collected by an unbiased unit cell in the ram mode. In all cases, cells on the corner collect more ions than cells along the line edge. The cells on the leading edge collect more ion current in the airplane mode than those on the trailing edge.

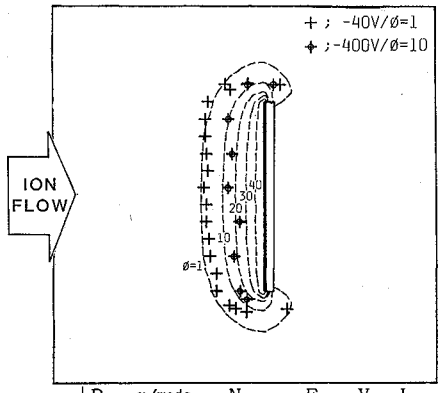

Fig. 7 Comparison between equipotential contours by the experiment and the calculation in the ram mode at 50% spanwise position; bold straight line, broken curves, and symbols represent solar array, numerical data, and experimental results using an emissive probe.

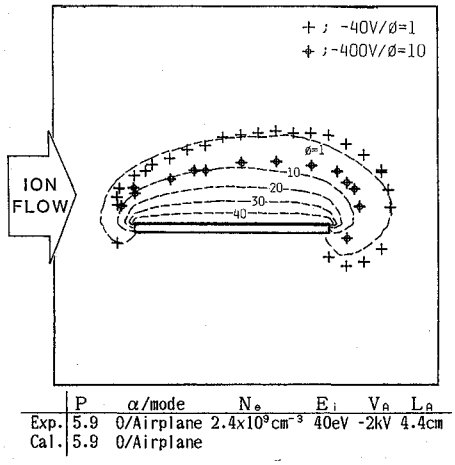

Fig. 8 Comparison between equipotential contours by the experiment and the calculation in the airplane mode at 50% spanwise position; bold straight line, broken curves, and symbols represent solar array, numerical data and experimental results using an emissive probe.

These results are in good agreement with the pattern of surface luminosity.

Discussion

Comparison with Calculation and Experiment

The results of the scale experiment include nonideal factors in the plasma environment as well as in measuring accuracy. The latter has already been described in the Scaled Experiment section. The effective plasma density depends on the array attitude and the extent of the ion sheath because of the nonuniformity along and across the ion beam. The accuracy, which is represented by the typical error bar in the figures, should be taken into account for the comparison of the numerical and the experimental results.

Ion Current

Agreement of the experimental results using two models with the same P parameter in Figs. 3 and 4 proves the validity of the similarity law. In addition, the numerical simulation describes quantitatively the ion current characteristics of the experiment. The ion current ratio shows enhancement of the ion current collected by the HVSA in the biased condition with respect to the ion saturation condition. In other words, it can be considered to be the area ratio of the ram sheath surface with respect to the array surface since the ions are collected from the sheath surface. This interpretation agrees with the physical meaning of Eq. (9).

The ion current dependence on the P parameter is different between the ram and the airplane modes as shown in Fig. 3 and explained as follows. In the case of the unbiased array, namely infinite P parameter, the ion current ratio is equal to

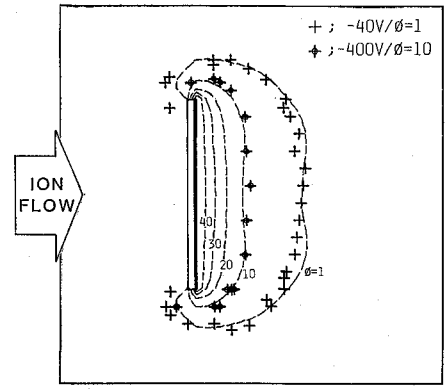

Fig. 9 Comparison between equipotential contours by experiment and calculation in the wake mode at 50% spanwise position; bold straight line, broken curves, and symbols represent solar array, numerical data, and experimental results using an emissive prove.

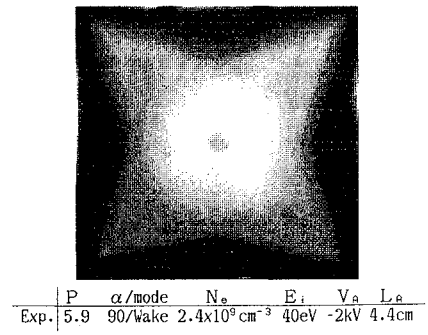

Fig. 10 Luminous pattern on the surface of the solar array model in the wake mode observed by a video camera; center shadow is a screw head.

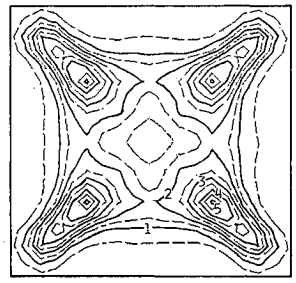

Fig. 11 Equicurrent density contours on the conductive surface in the wake mode obtained by the calculation.

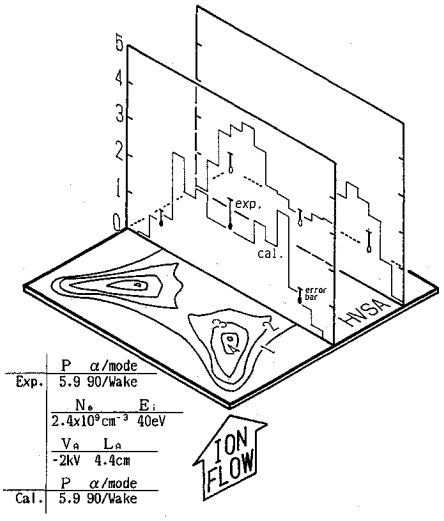

Fig. 12 Comparison of ion current density with the experiment and the calculation in the wake mode. Experimental data was measured using the segmented model.

unity for the ram mode, whereas the ratio equals zero for the airplane mode because of the vanishing frontal area of the model in the ion flow direction. Increasing the array potential or decreasing the array size decreases the P parameter and thickens the ion sheath covering the model so that both ion current curves merge gradually. This occurs because the ions are collected through the virtual surface area of the ion sheath instead of the physical surface of the HVSA. For the case of the airplane mode, the ion current is approximately proportional to the -0.5 power of the P parameter. The Child-Langmuir law indicates $D_i \propto V_A{}^{0.75}$, i.e., $D_i \propto P^{-0.5}$ because the ion current density is regarded as constant in LEO. The virtual surface area of the ion sheath is considered to be proportional to the first power of D_i owing to $D_i < L_A$ in the airplane orientation of Fig. 3. Therefore, the slope of the ion current characteristic in the airplane mode equals -0.5, closely obeying the law of Child-Langmuir, though slight deviation may occur due to three-dimensional effects. The ion current ratio also depends significantly on whether or not the insulated surface is directed toward the ram direction as can be seen in Fig. 4.

In case of a real HVSA having both conductors and insulators on its surface, the amount of collected ions will decrease in comparison to prediction from our results owing to reductions of ion sheath thickness and conductor area.

Ion Drag and Lift

The comparison between the numerical and the experimental results for drag and lift is represented in Fig. 5. The two results are in good agreement. The generation of thrust by the ion force is confirmed by the numerical and the experimental simulations as shown in Fig. 5. The ion particles with zero initial velocity, when viewed from the coordinate system fixed to the ionosphere, are accelerated by the array potential and collide with the HVSA. At this moment they are neutralized on the surface and leave the HVSA as atoms with large reflection velocity. The momentum difference between the incoming ion and the backscattering atom acts on the HVSA as an external force. When the backscattering atoms are ejected backward of the HVSA, the thrust is generated. In other words, the HVSA behaves like an ion engine using the ionospheric plasma as propellant and surface recombination as a neutralizer. Neutral particles sputtered from the HVSA by the ion collision also contribute to the production of the external force.

The ion force is found to be composed of F_{bs} due to backscattering and F_{sp} due to sputtering. Backscattering means reflection of the primary particle, whereas sputtering means ejection of the secondary. Their ratio is estimated as follows:

$$\frac{F_{sp}}{F_{bs}} = \frac{\gamma_{sp}}{\gamma_{bs}} \sqrt{\frac{m_{sp}E_{sp}}{m_{bs}E_{bs}}} \tag{16}$$

Inserting the values of these parameters,[13-15] F_{sp}/F_{bs} is found to be nearly unity. Although uncertainty exists due to lack of reliable data, it is found that both backscattering and sputtering contribute to the ion force.

In applying our results of the ion force to a real HVSA, the effects of the insulating cover glass must be taken into account. In addition to the decrease of collected ions, deflection of ion trajectory near the surface due to the complicated potential structure will reduce the magnitude of the ion force. However, the influence of the ion force should be included in mission analysis to estimate dynamics of a spacecraft equipped with HVSAs.

Potential Distribution

The ion sheath could be observed as a dark area because ions and atoms cannot be excited for lack of energetic electrons, as shown in Fig. 6. The luminescence from the excited particles must change drastically in the thermal sheath, which is very thin and is located between the uniform plasma and the ion space charge sheath. The border of the observed dark area, therefore, can be considered to be the edge of the ion sheath. The results obtained by the emissive probe can be compared with those by numerical simulation in Figs. 7, 8, and 9. The data of the emissive probe for -40 and -400 V correspond to the curves of $\phi = 1$ and $\phi = 10$, respectively, because of the 40-eV beam energy. They agree well with each other. The numerical simulation can thus describe the configuration variation of the sheath due to the ion beam orientation with respect to the HVSA.

Ion Current Distribution

The star-shaped luminosity on the model varied depending on the plasma density and the array potential. The thicker the ion sheath becomes, the more strongly the ion trajectories are deflected in the sheath so that a focusing effect[4] is observed.

The luminescent pattern in Fig. 10 resembles the pattern of the calculated ion current density in Fig. 11. Quantitative comparison between them cannot be carried out since there is no basis to make a correspondence between the luminosity and the current density. Figure 12, however, shows qualitative agreement between the calculation and the experiment in spite of low spatial resolution.

The numerical and the experimental simulations demonstrate that the corner portions of the HVSA collect a considerable amount of the ion current. The observation of the electrode erosion at corners supports this and generates concern about the endurance of a practical HVSA. As the operational voltage of a practical HVSA is lower than that of our experiment, the sputtering rate will be much less. But sputtering will

be an important issue for a long-lived mission, both from the point of view of material damage and of contamination to nearby surfaces.

Concluding Remarks

Initially, the scaling parameters were derived from the fundamental equations and interpreted physically. Next, a scaled experiment was conducted in the laboratory and validated the resulting similarity law. The test also verified that the numerical simulation code in Ref. 6 could describe quantitatively the interactions of the HVSA with the ionospheric plasma. In addition to the well-known interactions, the productions of an ion force and surface degradation by sputtering were confirmed experimentally and will affect a real HVSA in LEO. Some caution is, however, needed in directly applying our results to a practical HVSA owing to our simplifications for the scale experiment. Further studies will be needed. Anyway, the cooperative efforts of the flight experiment, numerical simulation, real-size experiment, and scaled experiment will reveal the plasma interactions of the HVSA.

References

[1]Stevens, N. J., "Review of Interactions of Large Space Structures with the Environment," *Progress in Astronautics and Aeronautics: Spacecraft Changing by Magnetospheric Plasmas*, edited by A. Rosen, AIAA, New York, 1975, pp. 437–453.

[2]Kuriki, K., Nagatomo, M., and Ijichi, K., "Energetic Experiment on Space Station," *Acta Astronautica*, Vol. 14, 1986, pp. 445–454.

[3]Katz, I., et al., "Plasma Collection by High-Voltage Spacecraft at Low Earth Orbit," *Journal of Spacecraft and Rockets,* Vol. 18, No. 1, 1981, pp. 79–82.

[4]McCoy, J. E., and Konradi, A., "Sheath Effects Observed on a 10 Meter High Voltage Panel in Simulated Low Earth Orbit Plasma," NASA CP-2071, 1978, pp. 315–340.

[5]Grier, N. T., and Stevens, N. J., "Plasma Interaction Experiment (PIX) Flight Results," NASA CP-2071, 1978, pp. 295–313.

[6]Kuninaka, H., and Kuriki, K., "Numerical Analysis on Interaction of a High Voltage Solar Array with the Ionospheric Plasma," *Journal of Spacecraft and Rockets,* Vol. 24, No. 6, 1987, pp. 512–517.

[7]Kuninaka, H., et al., "Interaction of High Voltage Solar Array with Ionospheric Plasma," International Electric Propulsion Conference, IEPC 88-016, Garmish-Partenkirshen, FRG, 1988.

[8]Johnson, F. S. (ed.), *Satellite Environment Handbook,* Stanford Univ., Stanford, CA, 1965, Chap. 2.

[9]Kuninaka, H., Nozaki, Y., and Kuriki, K., "High Voltage Solar Array Interacting with Ionospheric Plasma," *Space Power,* Vol. 8, No. 1 and 2, 1989, pp. 51–68.

[10]Ijichi, K., et al., "High Voltage Solar Array for MPD Propulsion System," AIAA Paper 85-2047, Sept. 1985.

[11]Kaminsky, M., "Atomic and Ionic Impact Phenomena on Metal Surface," Springer-Verlag, New York, 1965, Chap. 14.

[12]Yamagiwa, Y., and Kuriki, K., "Experimental Study of Double Stage Discharge Hall Ion Thruster," International Electric Propulsion Conference, IEPC 88-083, Garmish-Partenkirshen, FRG, 1988.

[13]Verbeek, H., Eckstein, W., and Bhattacharya, R. S., "Angular and Energy Distributions of H and He Atoms Backscattered from Gold," *Journal of Applied Physics,* Vol. 51, No. 3, 1980, pp. 1783–1789.

[14]Bader, M., Witteborn, F. C., and Snouse, T. W., "Sputtering of Metals by Mass-Analyzed N_2^+ and N^+," NASA TR R-105, 1961.

[15]Kruger, W., and Scharmann, A., "The Mean Velocity of Particles Ejected from a Polycrystalline Copper Surface During the Bombardment with High Energetic Ar^+-Ions," *Zeitschrift für Physik,* Bd. 237, 1970, pp. 263–271.

Henry B. Garrett
Associate Editor